

# Multi-scale Restoration of Missing Data in Optical Time-series Images with Masked Spatial-Temporal Attention Network

Zaiyan Zhang, *Student Member, IEEE*, Jining Yan, *Senior Member, IEEE*, Yuanqi Liang, Jiaxin Feng, Haixu He, and Wei Han, *Member, IEEE*

**Abstract**—Due to factors such as thick cloud cover and sensor limitations, remote sensing images often suffer from significant missing data, resulting in incomplete time-series information. Existing methods for imputing missing values in remote sensing images do not fully exploit spatio-temporal auxiliary information, leading to limited accuracy in restoration. Therefore, this paper proposes a novel deep learning-based approach called MS<sup>2</sup>TAN (Multi-scale Masked Spatial-Temporal Attention Network), for reconstructing time-series remote sensing images. Firstly, we introduce an efficient spatio-temporal feature extractor based on Masked Spatial-Temporal Attention (MSTA), to obtain high-quality representations of the spatio-temporal neighborhood features in the missing regions. Secondly, a Multi-scale Restoration Network consisting of the MSTA-based Feature Extractors, is employed to progressively refine the missing values by exploring spatio-temporal neighborhood features at different scales. Thirdly, we propose a “Pixel-Structure-Perception” Multi-Objective Joint Optimization method to enhance the visual effects of the reconstruction results from multiple perspectives and preserve more texture structures. Furthermore, the proposed method reconstructs missing values in all input temporal phases in parallel (i.e., Multi-In Multi-Out), achieving higher processing efficiency. Finally, experimental evaluations on two typical missing data restoration tasks across multiple research areas demonstrate that the proposed method outperforms state-of-the-art methods with an improvement of 0.40dB/1.17dB in mean peak signal-to-noise ratio (mPSNR) and 3.77%/9.41% in mean structural similarity (mSSIM), while exhibiting stronger texture and structural consistency.

**Index Terms**—missing data restoration, time-series remote sensing images, masked spatial-temporal attention, multi-scale restoration, multi-objective joint optimization.

## I. INTRODUCTION

OVER the past few decades, remote sensing data has been extensively used in various industries. Among them, high spatial resolution remote sensing imagery is particularly beneficial for applications such as vegetation monitoring, land cover mapping, and land cover change detection. However, the fine spatial resolution images suffer from inevitable information loss caused by internal factors (e.g., sensor malfunction) and external factors (e.g., atmospheric conditions), which restrict their applications in different domains [1].

(Corresponding author: Jining Yan.)

Z. Zhang, J. Yan, Y. Liang, J. Feng, H. He and W. Han are with the School of Computer Science, China University of Geosciences, Wuhan, 430074, China and also with Hubei Key Laboratory of Intelligent Geo-Information Processing, China University of Geosciences, Wuhan, 430074, China (e-mail: zzaiyan@cug.edu.cn; yanjn@cug.edu.cn; naji@cug.edu.cn; fjxpen1234@cug.edu.cn; 20161001925@cug.edu.cn; weihan@cug.edu.cn).

This paper addresses the issue of missing data in remote sensing image involving multiple spectra. Common tasks include resolving the Landsat-7 ETM+ sensor scan line corrector off (SLC-off) problem and removing thick clouds. The key challenge is to estimate the missing regions and fill the gaps with predicted pixels, ensuring visual and semantic consistency with the surrounding pixels to enhance data usability.

Researchers have proposed various methods to recover missing data in remote sensing images. Early approaches to missing value restoration can be broadly categorized into three types [1]: spatial-based, temporal-based, and spatio-temporal-based data recovery. These methods have shown promising results in specific scenarios with low resolution and low missing rates. However, most of them rely on linear models and struggle to handle complex and detailed scenes. Moreover, due to limited reference information, the generated images often exhibit blurriness and lack continuous textures.

In recent years, the rapid advancement of deep learning theory and computer hardware [2] has led to significant progress in remote sensing image restoration using deep learning-based methods. These methods can be broadly categorized into two types: CNN-based [3] and Transformer-based [4] approaches. Compared to traditional statistical models, CNNs exhibit strong non-linear expressive power, allowing for efficient extraction of spatial features from remote sensing data and significantly improving the accuracy of image restoration. However, these structures struggle to fully exploit time-series information, resulting in a bottleneck in restoration accuracy. Transformers, based on self-attention mechanisms, possess a global receptive field, enabling comprehensive and efficient utilization of both temporal sequences and images [5] to enhance reconstruction results [6]. However, due to the high resolution and long time-series of remote sensing images, token sequences become excessively long, leading to extremely high complexity in attention computations.

To efficiently mine spatio-temporal information in remote sensing images, we apply self-attention mechanism separately in the temporal and spatial dimensions and alternate between the two [7], greatly reducing computational complexity. To address the problem of significant distributional differences between missing and non-missing values in remote sensing images, we apply missing values mask and diagonal mask to the attention matrix [8], proposing Masked Spatial-Temporal Attention (MSTA) to enhance the expressive power of spatio-temporal attention and optimize the spectral discrepancy at the

transition regions.

For full exploitation of the spatio-temporal neighborhood features at different scales [9], we further propose a Multi-scale Restoration Network. The network consists of MSTA-based Feature Extractors with different embedding scales, which progressively refine the reconstruction of missing information from coarse to fine granularity levels, achieving higher restoration accuracy [10]. For model training, we propose a ‘‘Pixel-Structure-Perception’’ Multi-Objective Joint Optimization method, using pixel-wise loss as the basic loss for the restoration task and incorporating structural loss [11] and perceptual loss [12] to optimize the model’s results from the perspectives of structure, texture, shape, and spatial relations, thereby achieving high-quality image inpainting.

Finally, we conducted simulated and real data experiments to validate the performance of the proposed method for the ETM+ SLC-off and thick cloud removal tasks. The results from six research areas indicate that our method outperforms competitors. In addition, a validation study demonstrates the effectiveness of the core components.

In summary, our main contributions are as follows:

- 1) We propose a deep learning-based approach called MS<sup>2</sup>TAN, for repairing missing information in time-series remote sensing images. Our method utilizes a Multi-scale Restoration Network with MSTA-based Feature Extractors to learn the non-linear mapping between missing and complete data. Both simulated and real data experiments show that proposed MS<sup>2</sup>TAN outperforms state-of-the-art methods across multiple research areas.
- 2) To address the challenges of high resolution and long temporal sequences in remote sensing data, we introduce the Masked Spatial-Temporal Attention (MSTA) mechanism. The MSTA efficiently extracts spatio-temporal features, improves the utilization of spatio-temporal contextual information, reduces color transition artifacts at the boundaries of missing value regions, and significantly reduces the time complexity of self-attention.
- 3) For model training, we propose a ‘‘Pixel-Structure-Perception’’ Multi-Objective Joint Optimization method. This method considers pixel-wise reconstruction error, structural reconstruction error, and perceptual error, resulting in restoration results with enhanced visual quality and preserved texture and structural details.

The rest of this paper is organized as follows. In Section II, we review the existing methods for reconstructing missing information in remote sensing images. The network architecture and methodology details of our proposed model are presented in Section III. In Section IV, we showcase the results of missing data reconstruction in both simulated and real data experiments, compare them with mainstream methods, and validate the effectiveness of each component through validation study. Finally, our conclusions and future prospects are summarized in Section V.

## II. RELATED WORKS

### A. Traditional methods

Early research on the restoration of missing data in remote sensing images can be roughly divided into three cat-

egories: spatial-based, temporal-based, and spatio-temporal hybrid methods.

1) *Spatial-based Methods*: Spatial-based methods rely solely on the valid information within the image itself to predict the missing data. The most commonly used approach is spatial interpolation methods [13]. Additionally, methods based on partial differential equations (PDE) [14] and variational methods [15]–[17] have also been utilized for reconstructing missing values. Furthermore, patch-based methods have found extensive application [18]–[20]. In general, spatial-based methods are suitable for reconstructing small missing areas or regions with regular textures. However, the accuracy of the reconstruction cannot be guaranteed, particularly for large regions or complex textures.

2) *Temporal-based Methods*: Temporal-based methods utilize observations of the same location at different times from satellites to restore missing data. These methods include histogram matching-based approaches [21], temporal interpolation-based methods [22], replacement-based methods [23], and regression-based methods [24]–[26], among others. However, the differences between different time phases restrict the application of these methods.

3) *Spatio-temporal-based Methods*: To overcome these limitations, spatio-temporal-based methods integrate the spatial and temporal correlations to reconstruct missing data under various conditions. For instance, improved nearest neighbor pixel interpolation methods [27], methods based on spatio-temporal Markov random field model [28], spatio-temporal weighted regression model [29], methods based on group sparse representation [30], and methods based on low-rank tensor decomposition [31], [32] have been proposed. However, most of these methods rely on linear models and struggle to handle complex and intricate scenes.

### B. Deep learning-based methods

In recent years, deep learning methods based on CNN and Transformer have been widely applied.

1) *CNN-based methods*: CNNs have shown high efficiency in extracting spatial features from remote sensing data, leading to significant improvements in the accuracy of remote sensing image restoration. Malek et al. [33] applied a context encoder [34] to reconstruct thick clouds in remote sensing images. CNNs combined with GAN structures [35], [36] were used to generate realistic reconstructed images. Zhang et al. [37] proposed a CNN-based Spatio-Temporal Spectra (STS-CNN) framework, which was further developed into a progressive spatio-temporal patch grouping framework [38]. CNNs that incorporate temporal inputs through channel-wise concatenation [39] merge feature maps of target images and temporal images, introducing auxiliary information for missing data restoration. However, CNNs lack a true understanding of time series, which hinders the efficient integration of temporal and spatial information in these methods and limits the utilization of long temporal sequences as auxiliary information, ultimately affecting the restoration accuracy.

2) *Transformer-based methods*: Transformer [4] employs self-attention mechanism to process text sequences and capture global contextual information. It has been proven that

Transformer-based methods, such as Visual Transformer (ViT) [5], also exhibit powerful performance in the field of image processing. The sequence modeling capability of self-attention mechanism can be leveraged to assist in high-precision restoration of missing values in remote sensing images. Xu et al. [40] applied spatial self-attention to feature maps to capture the distribution of cloud thickness. Christopoulos et al. [41] utilized axial attention to remove thick clouds in remote sensing images. Recently, Liu et al. [42] used spatial attention and channel attention to remove cloud cover in the images. Li et al. [43] introduced SAR auxiliary data and synthesized cloud-free images using a Transformer-based GAN.

However, the spatial attention used in ViT requires computing the correlations between all pairs of patches. In the context of processing time-series remote sensing images, the images often have high resolutions and long time-series, resulting in a large number of tokens and extremely high computational complexity. Bertasius et al. [7] conducted a detailed comparison of various forms of spatial-temporal attention and proposed separated spatial-temporal attention that achieves a balance between efficiency and performance. We further improved the separated spatial-temporal attention by introducing missing value masks and diagonal masks [8], resulting in Masked Spatial-Temporal Attention (MSTA), which exhibits superior performance in the task of missing value restoration. Compared to CNN-based methods and original ViT methods, MSTA enables efficient processing of spatio-temporal information and leverages long-term temporal information to assist in missing value reconstruction, leading to more precise reconstruction results.

### III. METHODOLOGY

#### A. Problem Definition and Overall Framework

1) *Problem Definition:* The original time-series remote sensing image with missing values can be represented as  $X \in \mathbb{R}^{T \times C \times H \times W}$ , where  $T$  denotes the length of the time series,  $C$  represents the number of channels, and  $H$  and  $W$  denote the spatial dimensions of the region.  $X_{(t,c,i,j)}$  denotes the value of channel  $c$  at position  $(i, j)$  at time  $t$ . To account for the missing values, we introduce the missing value hint tensor  $M \in \mathbb{R}^{T \times C \times H \times W}$ , which is defined as shown in Equation (1). In practical applications, the missing value hint tensor  $M$  can be obtained from QA band or cloud detection algorithms such as Fmask [44].

$$M_{(t,c,i,j)} = \begin{cases} 0 & \text{if } X_{(t,c,i,j)} \text{ is missing,} \\ 1 & \text{if } X_{(t,c,i,j)} \text{ is observed.} \end{cases} \quad (1)$$

The target sequence  $Y$  in  $\mathbb{R}^{T \times C \times H \times W}$  represents the actual data, while  $\tilde{Y}$  in  $\mathbb{R}^{T \times C \times H \times W}$  represents the data repaired by the model. Therefore, the definition of the multi-temporal remote sensing image reconstruction model is given by equation (2). Here, the output  $\tilde{Y}$  of the model is the initial reconstruction result, and  $\odot$  denotes the Hadamard product. By replacing the observed real values in  $X$  with  $\tilde{Y}$ , we obtain the final reconstruction result  $\tilde{Y}_{\text{out}}$  as shown in equation (3).

$$\tilde{Y} = \text{Model}(X, M) \quad (2)$$

$$\tilde{Y}_{\text{out}} = \tilde{Y} \odot (1 - M) + X \odot M \quad (3)$$

Our objective is to make  $\tilde{Y}$  closely match the data distribution of  $Y$  in order to achieve high-quality reconstructed images.

2) *Overall Framework:* The proposed framework for time-series image recovery consists of a Multi-scale Restoration Network (called MS<sup>2</sup>TAN) with MSTA-based Feature Extractors and a ‘‘Pixel-Structure-Perception’’ Multi-Objective Joint Optimization method, as depicted in Fig. 1.

The framework utilizes the MS<sup>2</sup>TAN to learn the non-linear mapping from non-missing information to missing information. It employs the MSTA-based Feature Extractor (MFE) at different scales to extract temporal and spatial features for reconstruction. Finally, the network parameters are optimized using the ‘‘Pixel-Structure-Perception’’ Multi-Objective Joint Optimization method, and the trained parameters are used for inference. The details of these components will be discussed in the following sections III-B, III-C and III-D.

#### B. MSTA-based Feature Extractor

The structure of the MSTA-based Feature Extractor (MFE) module is illustrated in Fig. 2. It consists of position encoding and a cascade of  $L$  Masked Spatial-Temporal Attention (MSTA) units. The input to this module is a high-dimensional feature vector  $E \in \mathbb{R}^{TN \times d_{\text{emb}}}$ , which is obtained by embedding the time-series remote sensing image  $X$  and the missing information mask  $M$  into blocks (as described in detail in Section III-C1). Here,  $T$  represents the time-series length,  $N$  represents the number of patches in a single remote sensing image, and  $d_{\text{emb}}$  represents the dimension of the token vector corresponding to each patch. Subsequently, the position encoding introduces spatial-temporal positional semantics, followed by  $L$  layers of MSTA units, and ultimately produces a sequence with incorporated spatio-temporal correlation features.

1) *Masked Self-Attention:* The Transformer model utilizes self-attention mechanism to model sequences. It maps the input to query vector Q, key vector K, and value vector V. The attention score between Q and K is computed using Scaled Dot-Product, followed by the application of the Softmax function to obtain attention weights A. The final output is the attention-weighted V, as shown in Equation 4.

$$H = AV = \text{Softmax} \left( \frac{Q \cdot K^T}{\sqrt{d_k}} \right) \cdot V \quad (4)$$

where  $[Q, K, V] = X \cdot W_{\text{QKV}}$ .

To address the challenge of disparate distribution of missing values in remote sensing data and enhance feature extraction capability, we introduce missing value masks and diagonal masks into self-attention.

- The missing value mask sets the attention scores from patches with too high missing rate to other patches as  $-\infty$ , effectively masking the influence of missing values. This enables the model to focus on extracting useful information from non-missing data to fill in the gaps, without being affected by the missing data.
- The diagonal mask sets the diagonal of the attention matrix as  $-\infty$ , preventing each step from attending to

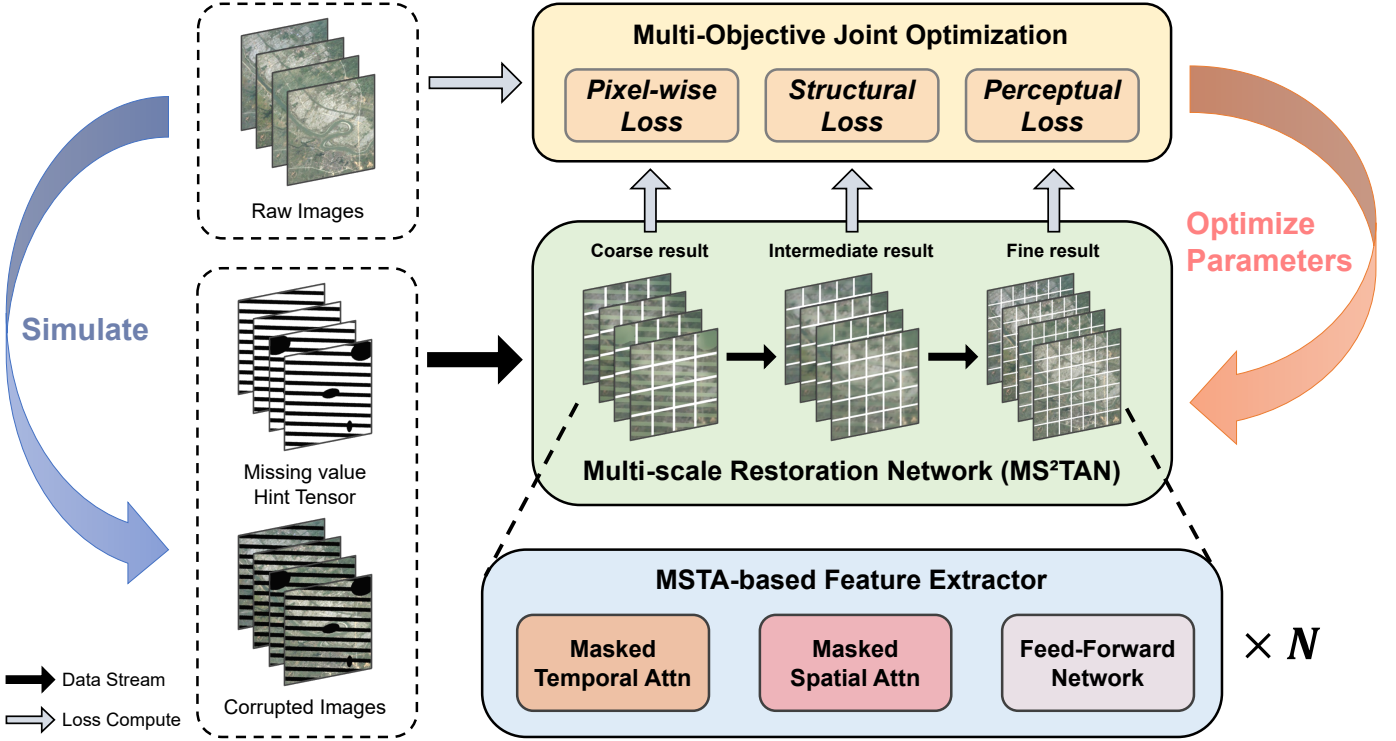


Fig. 1. The overall flowchart of the proposed method consists of two main components: a Multi-scale Restoration Network (named MS<sup>2</sup>TAN) with MSTA-based Feature Extractors, and a “Pixel-Structure-Perception” Multi-Objective Joint Optimization method.

itself and forcing it to rely on the other  $TN - 1$  steps for inference. This helps capture the spatio-temporal feature correlation in high-dimensional space.

More specifically, for the attention score matrix  $Sc \in \mathbb{R}^{TN \times TN}$ , the attention mask operation  $\text{ApplyMask}$  is defined as shown in Equation (5).

$$\text{ApplyMask}(Sc)_{(i,j)} = \begin{cases} -\infty & \text{Mask}(i,j) = 1, \\ Sc_{(i,j)} & \text{Mask}(i,j) \neq 1. \end{cases} \quad (5)$$

$$\text{Mask}(i,j) = 1 \text{ only if } (\text{MR}(E(i)) > C_{\max} \text{ or } i = j)$$

Here,  $\text{Mask}()$  checks whether the mask condition is satisfied,  $\text{MR}(e)$  represents the missing rate of the corresponding patch  $e$  (which can be calculated from the hint tensor  $M$ ), and  $C_{\max}$  is a hyperparameter that controls the maximum allowable missing rate. Applying Equation (5) to the attention scores in Equation (4), we obtain the expression for a single masked attention head, as shown in Equation (6). Finally, by linearly projecting and combining multiple attention heads with the residual connection, we obtain the output of the masked self-attention, as shown in Equation (7).

$$H^{(i)} = A'V = \text{Softmax} \left( \text{ApplyMask} \left( \frac{Q \cdot K^T}{\sqrt{d_k}} \right) \right) \cdot V \quad (6)$$

$$\text{MaskedAttn}(X, M) = \text{Proj} \left( \left[ H^{(1)}, H^{(2)}, \dots, H^{(h)} \right] \right) + X \quad (7)$$

In Equation (7),  $A'$  denotes the attention weights post mask application,  $\text{MaskedAttn}()$  represents the masked self-attention operation,  $\text{Proj}$  stands for projection head, and  $h$  denotes the number of attention heads.

2) *Masked Spatial-Temporal Attention*: Masked Spatial-Temporal Attention (MSTA) captures the spatio-temporal correlations within the input sequence, with its masking mechanism and receptive field depicted in Fig. 3. Specifically, MSTA comprises Masked Temporal Attention (MTA), Masked Spatial Attention (MSA), Layer Normalization (LN), and Feed-Forward Network (FFN). These components are elaborated upon below.

For an input sequence  $E \in \mathbb{R}^{TN \times d_{\text{emb}}}$ , MTA first reshapes  $E$  to place the time dimension and the feature dimension at the end, obtaining a sequence  $e_t$  of length  $T$  and  $d_{\text{emb}}$  dimensions. Subsequently, for each position in space, MaskedAttn operation is performed along the temporal direction to obtain the output of MTA, as shown in Equation (8).

$$e_t = \text{Reshape}(E) \in \mathbb{R}^{N \times T \times d_{\text{emb}}} \quad (8)$$

$$\text{MTA}(E, M) = \text{Reshape}(\text{MaskedAttn}(e_t, M))$$

Similarly, after the corresponding dimension transformation of the input sequence, MaskedAttn operation is conducted along the spatial direction for each temporal image, yielding the output of MSA, as shown in Equation (9).

$$e_s = \text{Reshape}(E) \in \mathbb{R}^{T \times N \times d_{\text{emb}}} \quad (9)$$

$$\text{MSA}(E, M) = \text{Reshape}(\text{MaskedAttn}(e_s, M))$$

FFN consists of two linear layers separated by a ReLU activation function, with a residual connection established between the input and output. The expression for FFN is presented in Equation (10).

$$\text{FFN}(X) = \text{Linear}(\text{ReLU}(\text{Linear}(X))) + X \quad (10)$$

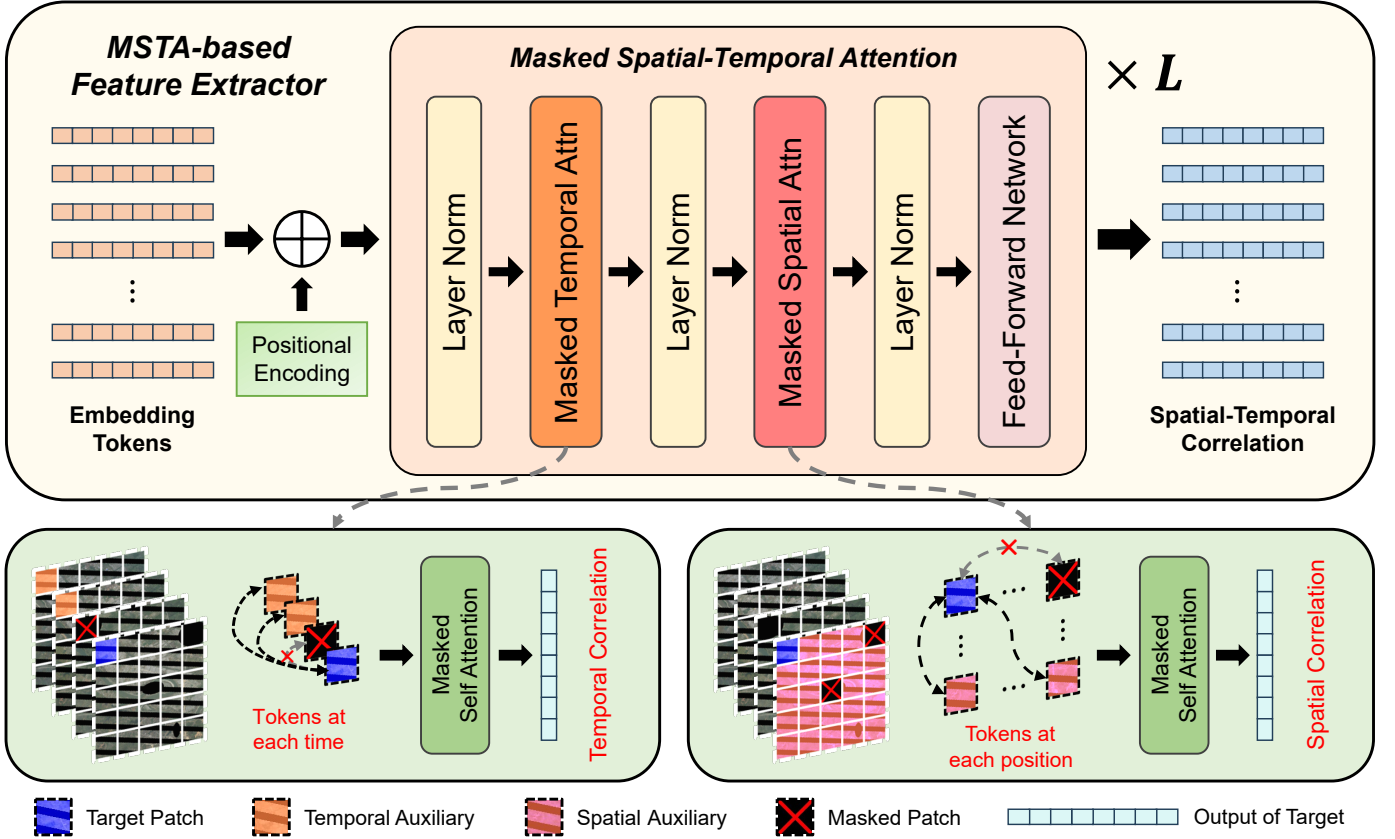


Fig. 2. Illustration of the structure of the MSTA-based Feature Extractor (MFE). The input sequence is augmented with positional encoding to incorporate positional information. It then undergoes  $L$  layers of Masked Spatial-Temporal Attention operations to obtain the output sequence, which combines temporal and spatial contextual features. The Masked Temporal/Spatial Attention, introduced below the image, respectively employ masked self-attention to capture the data distribution features in the Temporal/Spatial neighborhood.

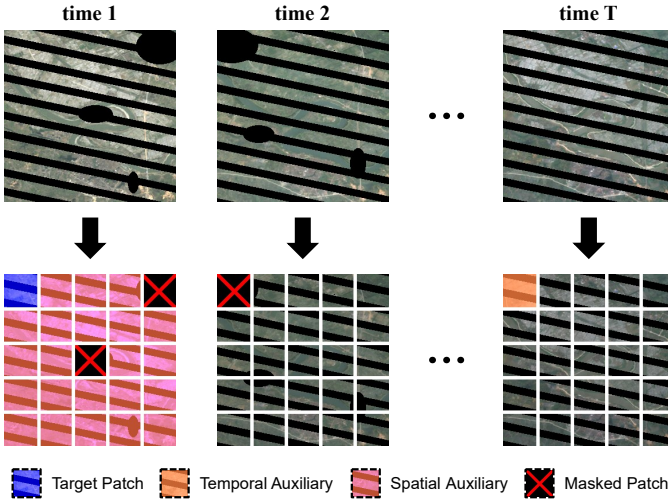


Fig. 3. Schematic of MSTA. Taking the blue patch as an example, patches at the same spatial position are considered as temporal auxiliaries, while patches at the same time are regarded as spatial auxiliaries. Additionally, patches with excessively high missing rates will be excluded from the receptive field to avoid the influence of distributional differences on model learning.

MSTA sequentially applies MTA and MSA to the input token sequence, exploring the spatio-temporal correlations among patches. Subsequently, FFN is used to fuse spatio-temporal features and introduce non-linear transformations, as

shown in Equation (11).

$$\begin{aligned}
 U &= \text{MTA}(\text{LN}(E), M) \\
 V &= \text{MSA}(\text{LN}(U), M) \\
 \text{MSTA}(E, M) &= \text{FFN}(\text{LN}(V))
 \end{aligned} \tag{11}$$

3) *Positional Encoding*: In the Transformer, positional encoding is added to the input sequence to introduce spatio-temporal positional semantics, as shown in Equation (12), where  $\text{PosEnc}(pos, dim)$  represents the value of the  $dim$ -th dimension of the positional encoding for the  $pos$ -th element in the sequence.

$$\begin{aligned}
 \text{PosEnc}(pos, 2i) &= \sin\left(pos \cdot 10000^{-2i/d_{\text{emb}}}\right) \\
 \text{PosEnc}(pos, 2i + 1) &= \cos\left(pos \cdot 10000^{-2i/d_{\text{emb}}}\right)
 \end{aligned} \tag{12}$$

After positional encoding, the input sequence will undergo  $L$  layers of MSTA to explore deeper spatio-temporal features. Finally, the overall expression of the MFE module is shown in Equation (13), where the symbol  $L$  denotes stacking  $L$  layers, and  $\text{MFE}()$  represents the MSTA-based Feature Extractor.

$$\text{MFE}(E, M) = \{\text{MSTA}(E + \text{PosEnc}, M)\}^L \tag{13}$$

### C. Multi-scale Restoration Network

The MS<sup>2</sup>TAN (Multi-Scale Masked Spatial-Temporal Attention Network) is a multi-scale restoration network com-

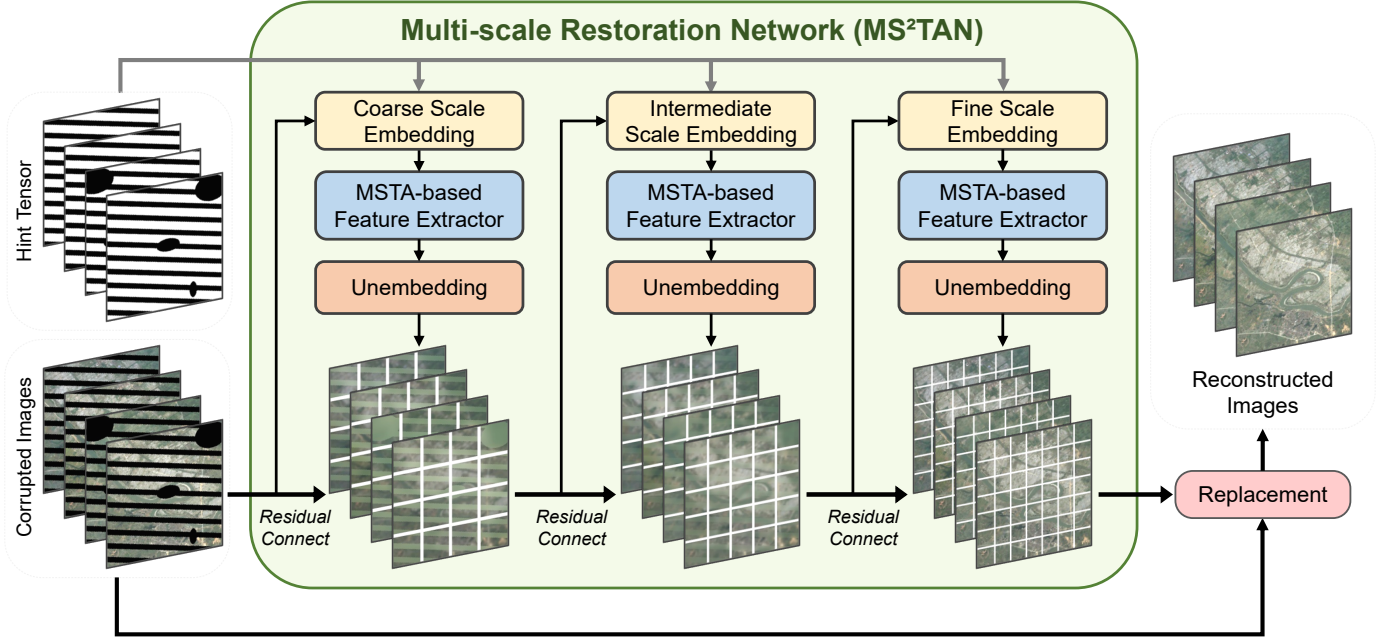


Fig. 4. The network structure diagram of proposed MS<sup>2</sup>TAN (Multi-Scale Masked Spatial-Temporal Attention Network), which includes components such as Embedding, MFE, Unembedding, and Observed Value Replacement.

posed of  $S$  residual-connected restoration modules and observed value replacement, as illustrated in Fig. 4. Each module consists of Patch Embedding, MFE, and Patch Unembedding. These restoration modules can capture the spatio-temporal correlations of pixels at different scales to predict missing values and ultimately replace observed values as outputs.

of each patch determined by the hyperparameter  $P$ . For each temporal image,  $N = HW/P^2$  patches are obtained. These patches are then aggregated and reorganized to form a patch sequence of length  $TN$ , with each patch represented as a  $C'P^2$ -dimensional vector. Equation (14) delineates the processing of the  $t$ -th temporal image  $x_c^t$ .

$$A^t = [p_1^t, p_2^t, \dots, p_N^t] = \text{Patchify}(x_c^t, P) \quad (14)$$

where  $x_c^t \in \mathbb{R}^{C' \times H \times W}$  and  $A^t \in \mathbb{R}^{N \times C'P^2}$

Next, a linear layer is utilized to project the vectors corresponding to each patch into a high-dimensional representation space. The images from different time steps are then aggregated to obtain the complete token sequence  $E$ , as depicted in Equation (15).

$$E^t = \text{Linear}(A^t) \in \mathbb{R}^{N \times d_{\text{emb}}} \quad (15)$$

$$E = [E^1, E^2, \dots, E^T] \in \mathbb{R}^{TN \times d_{\text{emb}}}$$

The process of transforming  $X_{\text{in}}$  and  $M$  step by step to obtain  $E$  as described above is referred to as Embedding, which can be represented by Equation (16). Conversely, if this operation is reversed, i.e.,  $E$  is restored to a patch sequence and then rearranged into an image, it is referred to as Unembedding, as shown in Equation (17). Fig. 5 illustrates the processes of Embedding and Unembedding on images.

$$E = \text{Embedding}(\text{Concat}(X_{\text{in}}, M), P) \quad (16)$$

$$X_{\text{out}} = \text{Unembedding}(E, P) \quad (17)$$

2) *MS<sup>2</sup>TAN*: MS<sup>2</sup>TAN consists of components such as Embedding, MFE, and Unembedding, where the block size  $P$  is an important hyperparameter, and the embedding scale of the  $i$ -th layer is denoted as  $P^{(i)}$ . The process of obtaining the embedding vector  $\alpha$  from the input is described in Equation

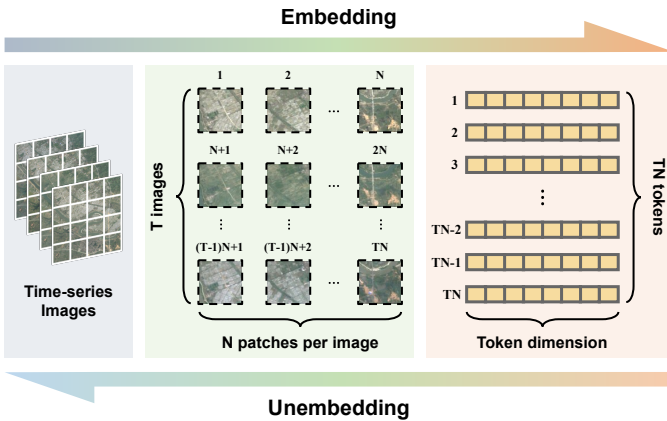


Fig. 5. Illustration of Embedding and Unembedding processes. Embedding represents a series of transformations from left to right, and Unembedding represents the reverse.

1) *Embedding and Unembedding*: The input to MS<sup>2</sup>TAN consists of two components: the image sequence  $X_{\text{in}}$  and the missing value hint tensor  $M$ . To incorporate the distributional properties of the missing values into the model learning process,  $X_{\text{in}}$  and  $M$  are concatenated along the channel dimension to yield the merged input  $X_c = \text{Concat}(X_{\text{in}}, M)$ , where  $X_c = [x_c^1, x_c^2, \dots, x_c^T] \in \mathbb{R}^{T \times C' \times H \times W}$ , where  $C' = C + 1$  is the total number of channels after concatenation.

Following the approach of Vision Transformer (ViT), each image is partitioned into a series of patches, with the size

(18). Subsequently, MFE is utilized to mine deep spatio-temporal correlation features  $\beta$ , as shown in Equation (19). Finally, the features are decoded, unembedded back into image form, and added to the input, resulting in an intermediate result as depicted in Equation (20), where  $\tilde{Y}^{(i)}$  represents the  $i$ -th intermediate result.

$$\alpha = \text{Embedding} \left( \text{Concat} \left( \tilde{Y}^{(i-1)}, M \right), P^{(i)} \right) \quad (18)$$

$$\beta = \text{MFE}(\alpha, M) \quad (19)$$

$$\tilde{Y}^{(i)} = \text{Unembedding} \left( \beta, P^{(i)} \right) + \tilde{Y}^{(i-1)} \quad (20)$$

Let  $\tilde{Y}^{(0)} = X_{\text{in}}$ , and sequentially obtain  $S$  intermediate results of the reconstruction. Eventually, the  $S$ -th result is taken as the output of MS<sup>2</sup>TAN, as shown in Equation (21).

$$\tilde{Y} = \text{MS}^2\text{TAN}(X_{\text{in}}, M) = \tilde{Y}^{(S)} \quad (21)$$

3) *Observed Value Replacement*: For the original reconstruction results of this network, denoted as  $\tilde{Y}$ , the observed values are replaced with their non-missing parts to obtain the final result  $\tilde{Y}_{\text{out}}$ , as shown in Equation (22).

$$\tilde{Y}_{\text{out}} = \tilde{Y} \odot (1 - M) + X \odot M \quad (22)$$

#### D. Multi-Objective Joint Optimization

To fully exploit the reconstruction capability of the model, this paper proposes a multi-objective joint optimization method to train the network parameters. This method utilizes the ‘‘Pixel-Structure-Perception’’ Multi-Objective Loss Function to optimize the results generated by the model from the perspectives of structure, color, texture, shape, and spatial relationships, achieving high-quality image inpainting.

1) *Pixel-wise Loss*: Pixel-wise loss disregards the overall integrity of the image, treating the image as a collection of pixels, and comparing pixel by pixel to generate the image against the target image. It serves as the foundational loss for remote sensing image reconstruction tasks. Specifically, Equation (23) illustrates its calculation process.

$$\mathcal{L}_{\text{pixel-wise}} = \frac{1}{TCHW} \|\eta - y\|_2^2 \quad (23)$$

The pixel-wise loss calculated here includes both missing and observed parts. The reduction of the loss in the observed part does not directly improve the performance of the model. However, it does smooth the model output, making the model training process more stable, and hence is also included.

2) *Structural Loss*: Pixel-wise reconstruction loss is commonly employed in various time-series and visual tasks but fails to consider the correlation between pixels. Structural reconstruction loss, based on the principle of structural similarity [45], measures the difference with the target image using the structural similarity index (SSIM), optimizing the visual consistency of the reconstruction results from the perspectives of structure, contrast, and luminance.

$$\begin{aligned} \mathcal{L}_{\text{structural}} &= 1 - \text{SSIM}(\eta, y) \\ &= 1 - \frac{(2\mu_\eta\mu_y + C_1)(2\sigma_{\eta y} + C_2)}{(\mu_\eta^2 + \mu_y^2 + C_1)(\sigma_\eta^2 + \sigma_y^2 + C_2)} \end{aligned} \quad (24)$$

Equation (24) specifies the computation process of structural loss, where  $\mu_\eta$  and  $\mu_y$  denote the means of  $\eta$  and  $y$  respectively,  $\sigma_\eta$  and  $\sigma_y$  denote the variances of  $\eta$  and  $y$  respectively,  $\sigma_{\eta y}$  denotes the covariance between  $\eta$  and  $y$ , and  $C_1$  and  $C_2$  are constants.

3) *Perceptual Loss*: Perceptual loss utilizes a pre-trained VGG16 network [46], as the feature extraction network to obtain perceptual feature vectors, followed by applying L2 loss to the feature vectors. The calculation of perceptual loss is shown in Equation (25), where  $\psi(\cdot)$  represents the feature extraction network, and  $d_f$  denotes the feature dimension.

$$\mathcal{L}_{\text{perceptual}} = \frac{1}{d_f} \|\psi(\eta) - \psi(y)\|_2^2 \quad (25)$$

4) *Multi-Objective Loss Function*: For each intermediate output  $\tilde{Y}^{(i)}$  of MS<sup>2</sup>TAN, the expression of the multi-objective loss function is shown in Equation (26), where  $\lambda_s$  and  $\lambda_p$  denote the weights of the structural loss and perceptual loss respectively. The final loss function considers the intermediate results of each layer, as shown in Equation (27).

$$\mathcal{L}^{(i)}(\eta, y) = \mathcal{L}_{\text{pixel-wise}} + \lambda_s \mathcal{L}_{\text{struct}} + \lambda_p \mathcal{L}_{\text{perceptual}} \quad (26)$$

$$\mathcal{L} = \frac{1}{S} \sum_{i=1}^m \mathcal{L}^{(i)}(\tilde{Y}^{(i)}, Y) \quad (27)$$

## IV. EXPERIMENT

### A. Experiment Settings

To assess the performance of the proposed algorithm, we conducted experiments on both simulated and real-world datasets. Additionally, we investigated the effectiveness of each core component of the proposed method.

1) *Datasets*: Different datasets were tailored for different missing data reconstruction tasks. For instance, for simulated ETM+ SLC-off and thick cloud removal tasks, we selected two research areas each for model training and testing. For real-world SLC-off and thick cloud removal, we chose one research area each and evaluated the trained model within them. All research areas comprised multiple images captured at different times. We employed a sliding window approach with a stride of 60 and a size of 120×120 to augment the sample amount, and then split them into training and testing sets. Specifically, Fig. 6 illustrates the spatial distribution and examples of each research area, while Table I provides detailed information on their data sources, tasks, time ranges, etc.

2) *Comparison Algorithms and Evaluation Metrics*: For the ETM+ SLC-off and thick cloud cover problems, we compared our method with LLHM [21], WLR [24], and STS-CNN [37]. These algorithms take a target image and a single temporal auxiliary image as input and synthesise a single reconstructed image, thus lacking the ability to handle long temporal auxiliary images, i.e., Dual-In Single-Out. In contrast, our proposed method leverages multi-temporal images with missing data as input and outputs reconstructed multi-temporal images in parallel, i.e., Multi-In Multi-Out. The simulated experiments utilized the mean peak signal-to-noise ratio (mPSNR) and the mean structural similarity index (mSSIM) for all spectral bands [6] as evaluation metrics. Furthermore, we repeated each

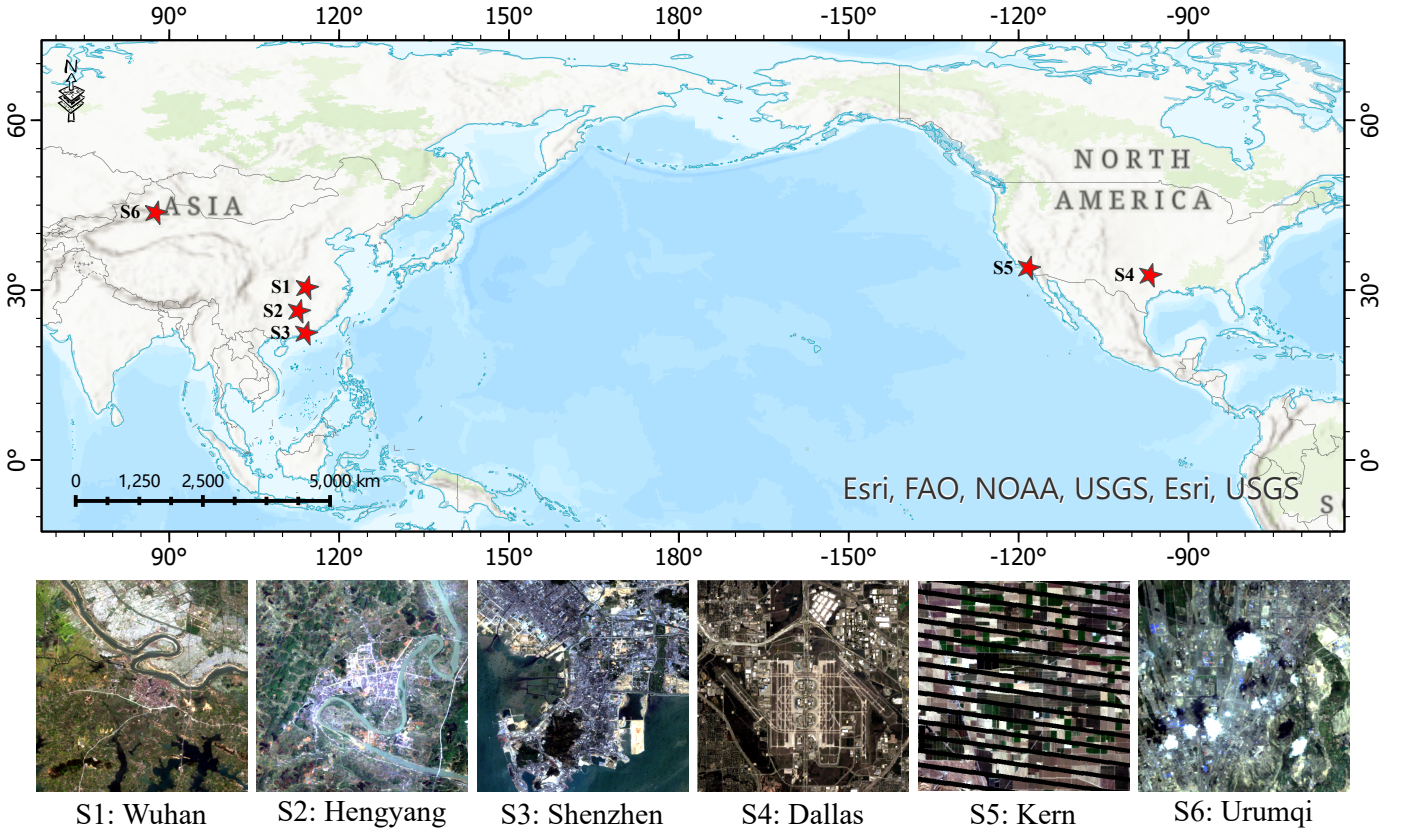


Fig. 6. The locations of the research areas used to evaluate the proposed methodology are shown with examples. S1 to S6 correspond to the locations of the six research areas in Table I: Wuhan, Hengyang, Shenzhen, Dallas, Kern, and Urumqi.

TABLE I  
DETAILS OF SIX RESEARCH AREAS

	Satellite	Task	Location	Date Range	Area Size and Resolution
S1	Landsat-5 TM	ETM+ SLC-off	Wuhan, Hubei, China	2001-03 to 2003-10	(1720, 2040) , 30-m
S2	Landsat-5 TM	ETM+ SLC-off	Hengyang, Hunan, China	2003-04 to 2005-05	(1200, 1200) , 30-m
S3	Landsat-5 TM	Thick Cloud Removal	Shenzhen, Guangdong, China	2003-10 to 2004-11	(1680, 1680) , 30-m
S4	Landsat-8 OLI	Thick Cloud Removal	Dallas, Texas, United States	2014-01 to 2014-11	(2040, 2040) , 30-m
S5	Landsat-7 ETM+	<b>Real</b> ETM+ SLC-off	Kern, California, United States	2011-09 to 2011-11	(1720, 2040) , 30-m
S6	Landsat-5 TM	<b>Real</b> Thick Cloud Removal	Urumqi, Xinjiang, China	2006-06 to 2009-08	(1440, 1440) , 30-m

experiment 5 times and used the average results as the final evaluation metric.

3) *Implement Detail*: For deep learning-based models, we utilized the Adam optimizer with parameters ( $\beta_1 = 0.9$ ,  $\beta_2 = 0.999$ ) for training, and set the batch size to 8. The initial learning rate was set to  $4 \times 10^{-4}$ , with a decay schedule of every 100 epochs, and an early stopping strategy of 30 epochs on the validation set to prevent overfitting. The proposed MS<sup>2</sup>TAN was implemented with PyTorch 1.12 framework and trained with a NVIDIA GeForce RTX3090 24GB GPU on a Ubuntu 20.04 environment. Additionally, the test code of MS<sup>2</sup>TAN is openly available on the Github at <https://github.com/zzaiyan/MS2TAN>.

## B. Simulated Experiment

1) *Simulated ETM+ SLC-Off Restoration Experiment*: For the land satellite ETM+ SLC-Off problem, we conducted sim-

ulated experiments with synthesized missing data in research areas S1 and S2, as illustrated in Fig. 7-8. In these figures, (a) and (b) represent the original image and the simulated SLC-off image, respectively, while (c)-(f) show the simulated recovery results using four methods—LLHM, WLR, STS-CNN, and the proposed MS<sup>2</sup>TAN. To provide a clearer view of the recovery results, we present magnified details next to each reconstruction. As shown in Fig. 7-8 (c)-(e), all compared methods generate discontinuous fine features to some extent. This is because the temporal auxiliary images cannot fully cover the missing regions, thus requiring LLHM and WLR algorithms to rely on LPRM to fill the remaining gaps, resulting in highly blurred noise bands in the reconstructed results. Although the STS-CNN model based on an end-to-end strategy can repair these gaps, it still cannot accurately restore the original features. In contrast, the proposed MS<sup>2</sup>TAN, utilizing a Masked Spatial-Temporal Attention mechanism

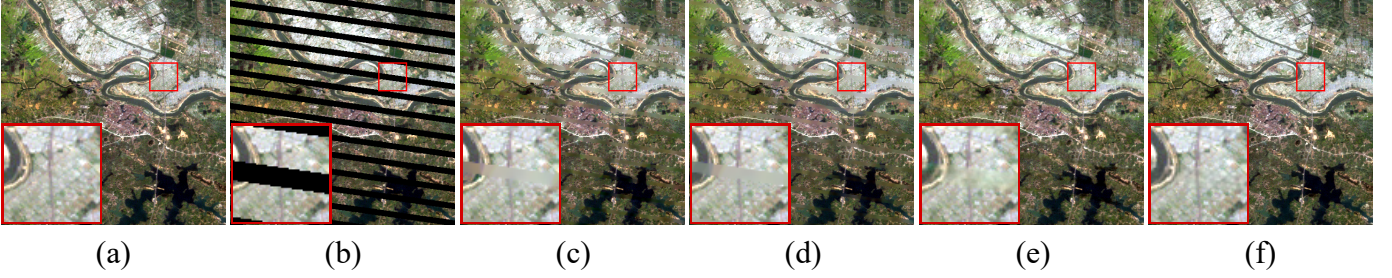


Fig. 7. Experimental results of Simulated ETM+ SLC-off Restoration based on Research Area S1. (a) Ground truth (March 19, 2002). (b) Simulated ETM+ SLC-off. (c) LLHM+LPRM. (d) WLR+LPRM. (e) STS-CNN. (f) Ours.

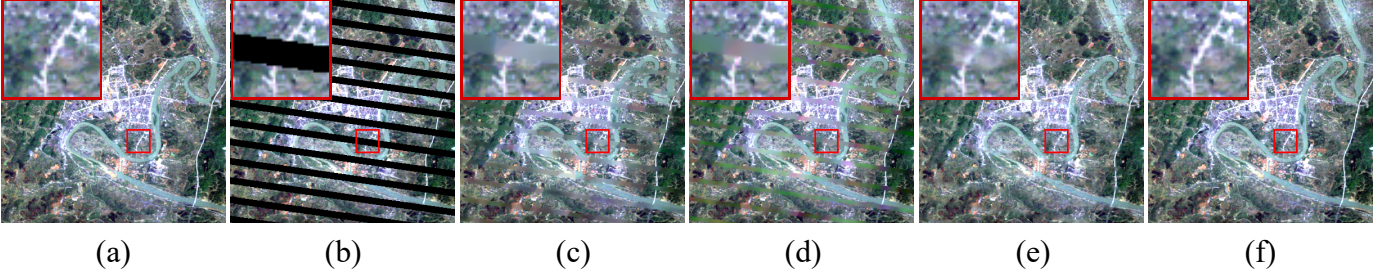


Fig. 8. Experimental results of Simulated ETM+ SLC-off Restoration based on Research Area S2. (a) Ground truth (April 15, 2003). (b) Simulated ETM+ SLC-off. (c) LLHM+LPRM. (d) WLR+LPRM. (e) STS-CNN. (f) Ours.

TABLE II  
QUANTITATIVE EVALUATION RESULT OF THE SIMULATED SLC-OFF RESTORATION IN RESEARCH AREA S1 AND S2

Dataset Metric	Area S1		Area S2	
	mPSNR( $\uparrow$ )	mSSIM( $\uparrow$ )	mPSNR( $\uparrow$ )	mSSIM( $\uparrow$ )
LLHM [21]	32.424	0.8947	32.908	0.9049
WLR [24]	34.374	0.9179	34.498	0.9214
STS-CNN [37]	37.118	0.9446	37.761	0.9479
<b>MS<sup>2</sup>TAN (Ours)</b>	<b>38.255</b>	<b>0.9548</b>	<b>38.963</b>	<b>0.9555</b>

TABLE III  
QUANTITATIVE EVALUATION RESULT OF THE SIMULATED THICK CLOUD REMOVAL IN RESEARCH AREA S3 AND S4

Dataset Metric	Area S3		Area S4	
	mPSNR( $\uparrow$ )	mSSIM( $\uparrow$ )	mPSNR( $\uparrow$ )	mSSIM( $\uparrow$ )
LLHM [21]	34.775	0.9439	34.714	0.9370
WLR [24]	39.003	0.9639	38.261	0.9614
STS-CNN [37]	39.515	0.9711	38.753	0.9662
<b>MS<sup>2</sup>TAN (Ours)</b>	<b>39.802</b>	<b>0.9753</b>	<b>39.272</b>	<b>0.9693</b>

and integrating a “Pixel-Structure-Perception” Multi-Objective Optimization approach, achieves better restoration of texture and structural details, as shown in Fig. 7-8 (f). Moreover, this method outperforms state-of-the-art methods in the quantitative evaluations presented in Table II, validating its strong capability in spatio-temporal integrated data utilization.

2) *Simulated Thick Cloud Removal Experiment*: Similar to the simulated experiments of ETM+ SLC-off, we simulated thick cloud removal tasks in research areas S3 and S4, and reconstructed the data using the same four methods, resulting in the outcomes shown in Fig. 9-10. Among them, LLHM exhibits severe texture discontinuities, while WLR produces numerous noise points. This is because these simple models struggle to handle highly complex nonlinear relationships between different times. In comparison, the STS-CNN model can more accurately reconstruct the texture and structural features of missing parts, but exhibits noticeable spectral transition phenomena at the edges of missing value regions. On the other hand, the proposed MS<sup>2</sup>TAN method introduces missing value hint tensors into the learning process, enhancing the model’s capability to handle irregularly distributed missing values. Ultimately, it performs well in maintaining consistency

in texture, structure, and spectral properties, achieving the best metrics in the quantitative evaluation presented in Table III.

### C. Real Data Experiment

1) *SLC-off Restoration Experiment*: The experimental results of real SLC-off images in research area S5 are shown in Fig. 11. In this figure, (a) and (b) depict two ETM+ SLC-off images observed on October 23, 2011, and November 8, 2011, respectively, while (c)-(h) display the outputs of four algorithms. Similar to the simulated SLC-off reconstruction experiment, single temporal auxiliary images cannot fully cover the gaps. Thus, after LLHM and WLR processing, the remaining gaps are filled using the LPRM algorithm. STS-CNN can directly repair the entire image but exhibits discontinuous texture features similar to the simulated experiment. Thanks to the “Pixel-Structure-Perception” Multi-Objective Joint Optimization method, the proposed MS<sup>2</sup>TAN method preserves more structural details and produces more consistent reconstruction results.

2) *Thick Cloud Removal Experiment*: The experimental results of thick cloud coverage reconstruction in region S6 are

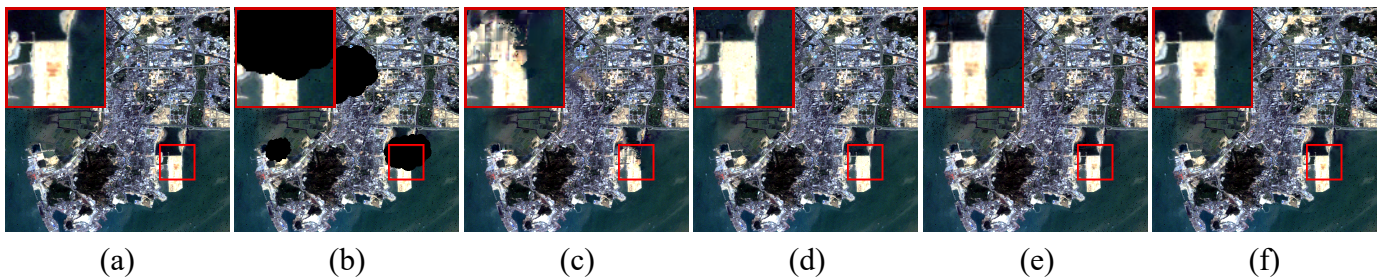


Fig. 9. Experimental results of Simulated Thick Cloud Removal based on Research Area S3. (a) Ground truth (October 17, 2003). (b) Simulated Thick Cloud. (c) LLHM. (d) WLR. (e) STS-CNN. (f) Ours.

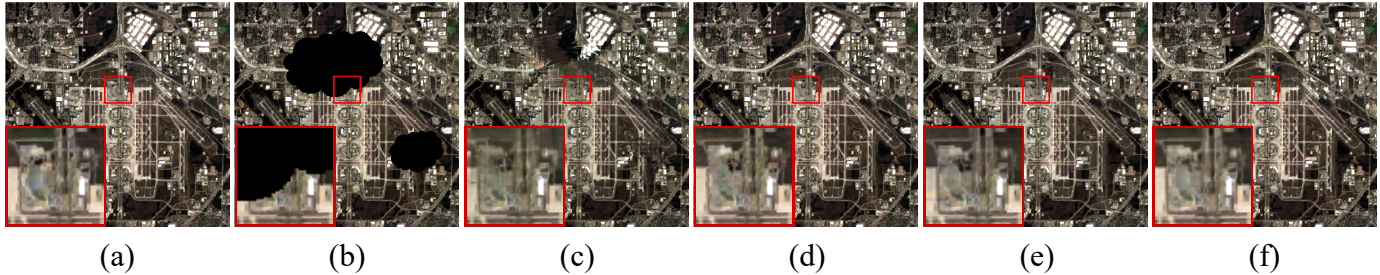


Fig. 10. Experimental results of Simulated Thick Cloud Removal based on Research Area S4. (a) Ground truth (January 22, 2014). (b) Simulated Thick Cloud. (c) LLHM. (d) WLR. (e) STS-CNN. (f) Ours.

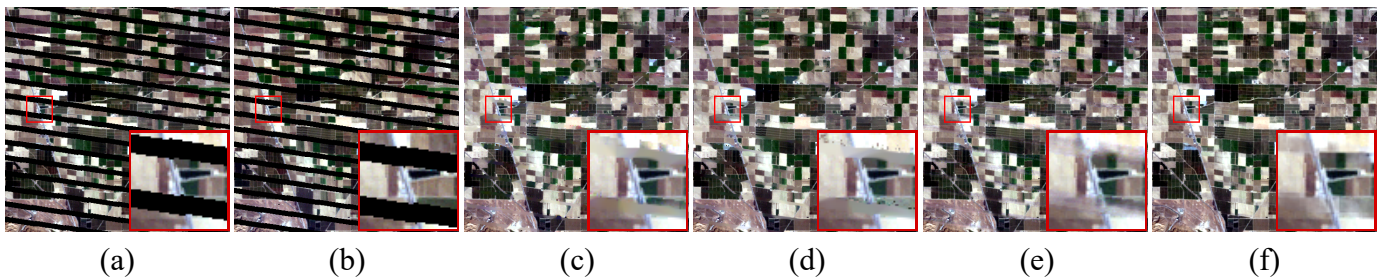


Fig. 11. Experimental results of **Real** ETM+ SLC-off Restoration based on Research Area S5. (a) SLC-off Image 1 (October 23, 2011). (b) SLC-off Image 2 (November 8, 2011). (c) LLHM+LPRM. (d) WLR+LPRM. (e) STS-CNN. (f) Ours.

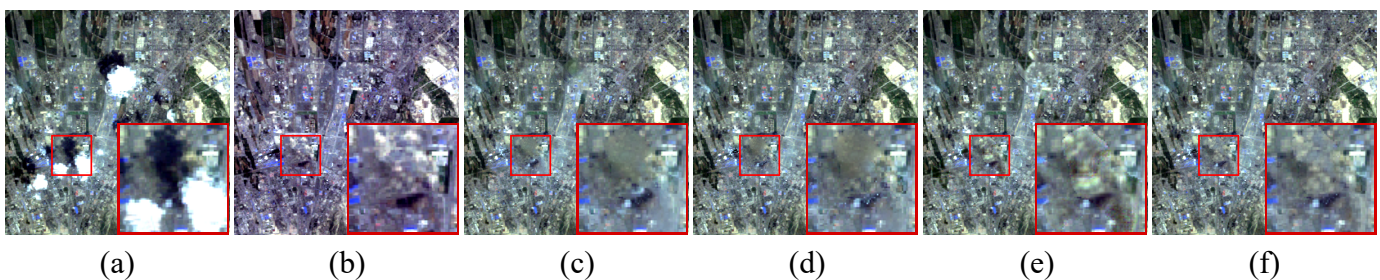


Fig. 12. Experimental results of **Real** Thick Cloud Removal based on Research Area S6. (a) Image with clouds (August 5, 2007). (b) Temporal image without clouds (July 20, 2007). (c) LLHM. (d) WLR. (e) STS-CNN. (f) Ours.

shown in Fig. 12. In Fig. 12 (a), an image containing thick clouds is presented, while (b) depicts the temporal auxiliary image. Four algorithms identical to those used in the SLC-off reconstruction experiment were employed to reconstruct the images, yielding results displayed in (c)-(f). It can be observed in Fig. 12 (a)-(b) that for extensive cloud coverage and cloud shadows, the results of LLHM and WLR models suffer from significant loss of texture and structural features, presenting as blurry patches. This is attributed to the inconsistency between

the reconstructed texture details in the cloud region and the surrounding non-cloud areas, which the aforementioned models fail to fit due to their incapability to capture the nonlinear relationship between different temporal data. In comparison, the STS-CNN method exhibits better performance in texture restoration, yet still shows noticeable spectral discontinuities at the boundaries of missing regions. On the other hand, the proposed MS<sup>2</sup>TAN method fully preserves texture and structural details with less spectral distortion compared to STS-CNN,

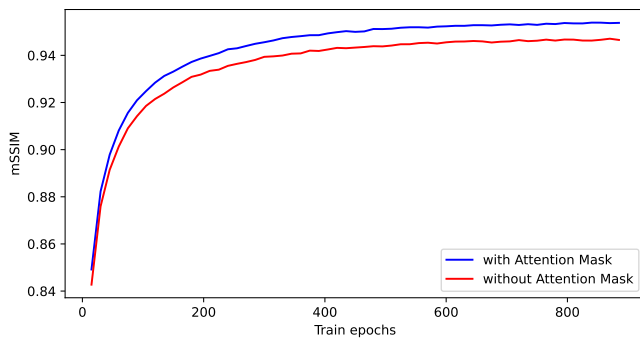


Fig. 13. Ablation experiments for the proposed MSTA mechanism. The blue and red curves respectively depict the variations of mSSIM with training rounds for models with and without the adoption of the attention mask mechanism in Area S1.

resulting in high-quality thick cloud removal images.

#### D. Validation Study

1) *Masked Spatial-Temporal Attention*: To validate the effectiveness of the proposed Masked Spatial-Temporal Attention (MSTA) mechanism, we compared models with and without the adoption of this mechanism, and plotted their mSSIM iteration curves on the validation set, as shown in Fig. 13. It can be observed that with the assistance of the attention mask mechanism, the model exhibits faster convergence speed and higher fitting accuracy. This confirms that the attention mask mechanism effectively enhances the model's feature extraction capability and training speed.

2) *Multi-scale Restoration*: The MS<sup>2</sup>TAN employs a multi-scale restoration strategy to process input images. To validate its effectiveness, we take the SLC-off reconstruction task as an example and compare the intermediate outputs of each layer. The results are shown in Fig. 14. In the figure, the missing regions of the input image are filled with zeros. After Coarse Embedding, MFE, and Unembedding, a coarse repair result is obtained. This result reconstructs most of the texture and structural features and balances the significant distribution differences between the missing regions and other areas in the input. However, there are still spectral discontinuities at the edges of the missing regions. After several layers of restoration, the final refined repair result is obtained. This result refines the previous intermediate results, with clearer textures, consistent spectra, and smoother integration of the repair area boundary with other areas.

3) *Gains from long time-series image inputs*: A highlight of the proposed model is its capability to utilize longer time-series images for assistance in restoration, leading to more accurate reconstruction results. We designed experiments to compare different lengths of time-series inputs to quantitatively evaluate the accuracy gains from longer time-series inputs. The experimental results are shown in Fig. 15. From Fig. 15, it can be observed that as the length of the input time series increases from 2, there is a significant improvement in mPSNR and mSSIM metrics. However, when the time series length reaches 5 or longer, the change in accuracy becomes less significant. Therefore, longer time-series inputs can significantly improve the accuracy of missing value reconstruction,

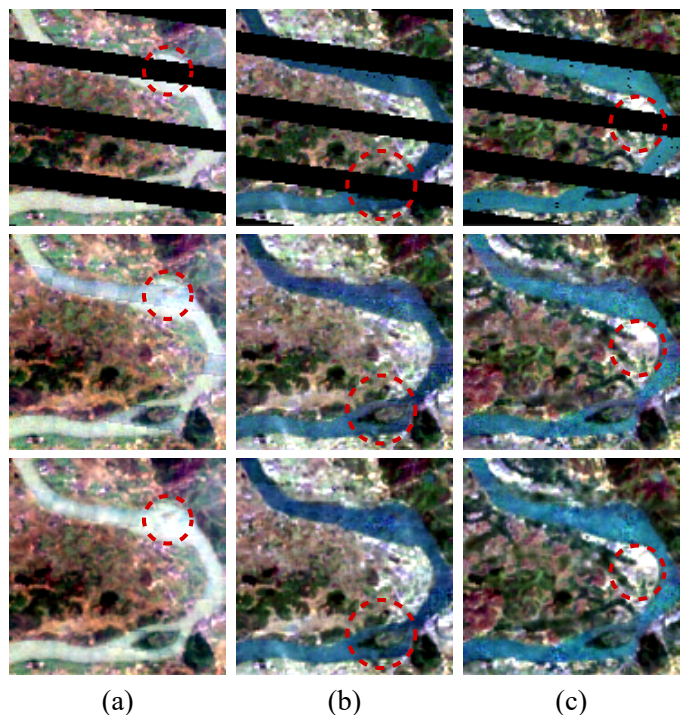


Fig. 14. Ablation experiments for multi-scale restoration. (a)-(c) represent observations from three different times, processed in parallel by MS<sup>2</sup>TAN after composing the time-series remote sensing images. From top to bottom, they represent: input with missing values, coarse result, and fine result.

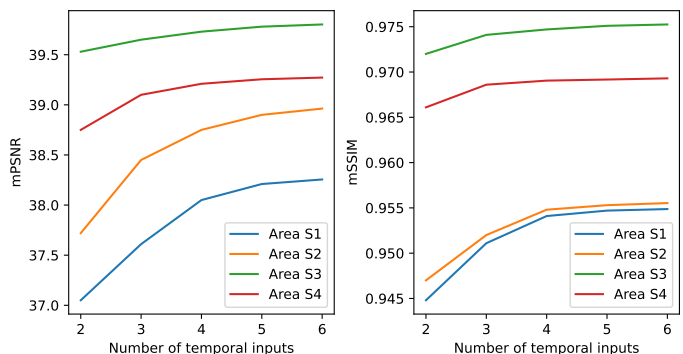


Fig. 15. Analysis of the input time-series length. The left and right tables record the variations of mPSNR and mSSIM with the length of the time-series, respectively, and distinguish the results of four research areas with different colors.

but there is a certain limit. Hence, we can find a balance point between reconstruction accuracy and algorithm flexibility.

## V. CONCLUSION

In this paper, we proposed a novel method for time-series remote sensing image reconstruction based on a Multi-scale Masked Spatial-Temporal Attention Network. The proposed method reconstructs various missing value scenarios, including the Landsat ETM+ SLC-off problem and removal of thick cloud coverage in remote sensing images. Compared to existing methods, the proposed method improves the efficiency of spatio-temporal information utilization, enabling the mutual assistance of multiple degraded time-series images for reconstruction and achieving higher restoration accuracy through

more auxiliary information. Additionally, the application of the MSTA mechanism and Multi-Objective Joint Optimization further enhances the texture and structural consistency of the reconstruction results. Experimental results demonstrate significant improvements in visual effects and restoration accuracy compared to mainstream methods.

Although the proposed method performs well in reconstructing the ETM+ SLC-off problem and thick cloud removal, there are still some inevitable limitations. For example, the model needs to simulate various shapes of cloud-like missing regions in the dataset and learn the characteristics of missing value distribution extraction sufficiently to achieve better cloud removal effects, which requires more training time for the model. In our future research, we can incorporate network components pre-trained on large-scale datasets into the model to improve its convergence speed.

#### ACKNOWLEDGMENTS

This work was supported in part by the National Key R&D Program of China (Project No. 2022YFC3800700); in part by the National Natural Science Foundation of China (No. U21A2013).

#### REFERENCES

- [1] H. Shen, X. Li, Q. Cheng, C. Zeng, G. Yang, H. Li, and L. Zhang, "Missing information reconstruction of remote sensing data: A technical review," *IEEE Geosci. Remote Sens. Mag.*, vol. 3, no. 3, pp. 61–85, 2015.
- [2] Y. LeCun, Y. Bengio, and G. Hinton, "Deep learning," *nature*, vol. 521, no. 7553, pp. 436–444, 2015.
- [3] Y. LeCun, B. Boser, J. Denker, D. Henderson, R. Howard, W. Hubbard, and L. Jackel, "Handwritten digit recognition with a back-propagation network," *Proc. Adv. Neural Inf. Process. Syst.*, vol. 2, 1989.
- [4] A. Vaswani, N. Shazeer, N. Parmar, J. Uszkoreit, L. Jones, A. N. Gomez, L. Kaiser, and I. Polosukhin, "Attention is all you need," *Proc. Adv. Neural Inf. Process. Syst.*, vol. 30, 2017.
- [5] A. Dosovitskiy, L. Beyer, A. Kolesnikov, D. Weissenborn, X. Zhai, T. Unterthiner, M. Dehghani, M. Minderer, G. Heigold, S. Gelly *et al.*, "An image is worth 16x16 words: Transformers for image recognition at scale," in *Proc. Int. Conf. Learn. Represent.*, 2020.
- [6] H. Shen, X. Meng, and L. Zhang, "An integrated framework for the spatio-temporal-spectral fusion of remote sensing images," *IEEE Trans. Geosci. Remote Sens.*, vol. 54, no. 12, pp. 7135–7148, 2016.
- [7] G. Bertasius, H. Wang, and L. Torresani, "Is space-time attention all you need for video understanding?" in *Proc. Int. Conf. Mach. Learn.*, vol. 2, no. 3, 2021, p. 4.
- [8] W. Du, D. Côté, and Y. Liu, "Saits: Self-attention-based imputation for time series," *Expert Systems with Applications*, vol. 219, p. 119619, 2023.
- [9] C. Yang, X. Lu, Z. Lin, E. Shechtman, O. Wang, and H. Li, "High-resolution image inpainting using multi-scale neural patch synthesis," in *Proc. IEEE Conf. Comput. Vis. Pattern Recognit.*, 2017, pp. 6721–6729.
- [10] K. He, X. Zhang, S. Ren, and J. Sun, "Deep residual learning for image recognition," in *Proc. IEEE Conf. Comput. Vis. Pattern Recognit.*, 2016, pp. 770–778.
- [11] H. Zhao, O. Gallo, I. Frosio, and J. Kautz, "Loss functions for image restoration with neural networks," *IEEE Trans. Comput. Imag.*, vol. 3, no. 1, pp. 47–57, 2016.
- [12] J. Johnson, A. Alahi, and L. Fei-Fei, "Perceptual losses for real-time style transfer and super-resolution," in *Proc. Eur. Conf. Comput. Vis.* Springer, 2016, pp. 694–711.
- [13] C. Zhang, W. Li, and D. Travis, "Gaps-fill of slc-off landsat etm+ satellite image using a geostatistical approach," *Int. J. Remote Sens.*, vol. 28, pp. 5103–5122, 11 2007.
- [14] M. Bertalmio, G. Sapiro, V. Caselles, and C. Ballester, "Image inpainting," in *Proceedings of the 27th Annual Conference on Computer Graphics and Interactive Techniques*. ACM Press/Addison-Wesley Publishing Co., 2000, pp. 417–424.
- [15] R. Hardie, K. Barnard, and E. Armstrong, "Joint map registration and high-resolution image estimation using a sequence of undersampled images," *IEEE Trans. Image Process.*, vol. 6, no. 12, pp. 1621–1633, 1997.
- [16] Q. Yuan, L. Zhang, and H. Shen, "Hyperspectral image denoising with a spatial-spectral view fusion strategy," *IEEE Trans. Geosci. Remote Sens.*, vol. 52, no. 5, pp. 2314–2325, 2014.
- [17] Q. Cheng, H. Shen, L. Zhang, and P. Li, "Inpainting for remotely sensed images with a multichannel nonlocal total variation model," *IEEE Trans. Geosci. Remote Sens.*, vol. 52, no. 1, pp. 175–187, 2014.
- [18] A. Criminisi, P. Perez, and K. Toyama, "Region filling and object removal by exemplar-based image inpainting," *IEEE Trans. Image Process.*, vol. 13, no. 9, pp. 1200–1212, 2004.
- [19] K. He and J. Sun, "Image completion approaches using the statistics of similar patches," *IEEE Trans. Pattern Anal. Mach. Intell.*, vol. 36, no. 12, pp. 2423–2435, 2014.
- [20] Q. Cheng, H. Shen, L. Zhang, and Z. Peng, "Missing information reconstruction for single remote sensing images using structure-preserving global optimization," *IEEE Signal Process. Lett.*, vol. 24, no. 8, pp. 1163–1167, 2017.
- [21] P. Scaramuzza and J. Barsi, "Landsat 7 scan line corrector-off gap-filled product development," in *Proceeding of Pecora*, vol. 16, 2005, pp. 23–27.
- [22] J. Chen, X. Zhu, J. E. Vogelmann, F. Gao, and S. Jin, "A simple and effective method for filling gaps in landsat etm+ slc-off images," *Remote Sens. Environ.*, vol. 115, no. 4, pp. 1053–1064, 2011.
- [23] G. Gao and Y. Gu, "Multitemporal landsat missing data recovery based on tempo-spectral angle model," *IEEE Trans. Geosci. Remote Sens.*, vol. 55, no. 7, pp. 3656–3668, 2017.
- [24] C. Zeng, H. Shen, and L. Zhang, "Recovering missing pixels for landsat etm+ slc-off imagery using multi-temporal regression analysis and a regularization method," *Remote Sens. Environ.*, vol. 131, pp. 182–194, 2013.
- [25] X. Li, H. Shen, L. Zhang, H. Zhang, Q. Yuan, and G. Yang, "Recovering quantitative remote sensing products contaminated by thick clouds and shadows using multitemporal dictionary learning," *IEEE Trans. Geosci. Remote Sens.*, vol. 52, no. 11, pp. 7086–7098, 2014.
- [26] J. Zhang, M. K. Clayton, and P. A. Townsend, "Missing data and regression models for spatial images," *IEEE Trans. Geosci. Remote Sens.*, vol. 53, no. 3, pp. 1574–1582, 2014.
- [27] X. Zhu, F. Gao, D. Liu, and J. Chen, "A modified neighborhood similar pixel interpolator approach for removing thick clouds in landsat images," *IEEE Geosci. Remote Sens. Lett.*, vol. 9, no. 3, pp. 521–525, 2011.
- [28] Q. Cheng, H. Shen, L. Zhang, Q. Yuan, and C. Zeng, "Cloud removal for remotely sensed images by similar pixel replacement guided with a spatio-temporal mrf model," *ISPRS J. Photogramm. Remote Sens.*, vol. 92, pp. 54–68, 06 2014.
- [29] B. Chen, B. Huang, L. Chen, and B. Xu, "Spatially and temporally weighted regression: A novel method to produce continuous cloud-free landsat imagery," *IEEE Trans. Geosci. Remote Sens.*, vol. 55, no. 1, pp. 27–37, 2016.
- [30] X. Li, H. Shen, H. Li, and L. Zhang, "Patch matching-based multitemporal group sparse representation for the missing information reconstruction of remote-sensing images," *IEEE J. Sel. Topics Appl. Earth Observ. Remote Sens.*, vol. 9, no. 8, pp. 3629–3641, 2016.
- [31] M. K.-P. Ng, Q. Yuan, L. Yan, and J. Sun, "An adaptive weighted tensor completion method for the recovery of remote sensing images with missing data," *IEEE Trans. Geosci. Remote Sens.*, vol. 55, no. 6, pp. 3367–3381, 2017.
- [32] H. He, J. Yan, L. Wang, D. Liang, J. Peng, and C. Li, "Bayesian temporal tensor factorization-based interpolation for time-series remote sensing data with large-area missing observations," *IEEE Trans. Geosci. Remote Sens.*, vol. 60, pp. 1–13, 2022.
- [33] S. Malek, F. Melgani, Y. Bazi, and N. Alajlan, "Reconstructing cloud-contaminated multispectral images with contextualized autoencoder neural networks," *IEEE Trans. Geosci. Remote Sens.*, vol. 56, no. 4, pp. 2270–2282, 2017.
- [34] D. Pathak, P. Krähenbühl, J. Donahue, T. Darrell, and A. A. Efros, "Context encoders: Feature learning by inpainting," in *Proc. IEEE Conf. Comput. Vis. Pattern Recognit.*, 2016, pp. 2536–2544.
- [35] L. Sun, Y. Zhang, X. Chang, Y. Wang, and J. Xu, "Cloud-aware generative network: Removing cloud from optical remote sensing images," *IEEE Geosci. Remote Sens. Lett.*, vol. 17, no. 4, pp. 691–695, 2019.
- [36] M. Shao, C. Wang, W. Zuo, and D. Meng, "Efficient pyramidal gan for versatile missing data reconstruction in remote sensing images," *IEEE Trans. Geosci. Remote Sens.*, vol. 60, pp. 1–14, 2022.

- [37] Q. Zhang, Q. Yuan, C. Zeng, X. Li, and Y. Wei, "Missing data reconstruction in remote sensing image with a unified spatial-temporal-spectral deep convolutional neural network," *IEEE Trans. Geosci. Remote Sens.*, vol. 56, no. 8, pp. 4274–4288, 2018.
- [38] Q. Zhang, Q. Yuan, J. Li, Z. Li, H. Shen, and L. Zhang, "Thick cloud and cloud shadow removal in multitemporal imagery using progressively spatio-temporal patch group deep learning," *ISPRS J. Photogramm. Remote Sens.*, vol. 162, pp. 148–160, 2020.
- [39] Y. Chen, L. Tang, X. Yang, R. Fan, M. Bilal, and Q. Li, "Thick clouds removal from multitemporal zy-3 satellite images using deep learning," *IEEE J. Sel. Topics Appl. Earth Observ. Remote Sens.*, vol. 13, pp. 143–153, 2019.
- [40] M. Xu, F. Deng, S. Jia, X. Jia, and A. J. Plaza, "Attention mechanism-based generative adversarial networks for cloud removal in landsat images," *Remote Sens. Environ.*, vol. 271, p. 112902, 2022.
- [41] D. Christopoulos, V. Ntouskos, and K. Karantza, "Cloudtran: Cloud removal from multitemporal satellite images using axial transformer networks," *The International Archives of the Photogrammetry, Remote Sensing and Spatial Information Sciences*, vol. 43, pp. 1125–1132, 2022.
- [42] H. Liu, B. Huang, and J. Cai, "Thick cloud removal under land cover changes using multisource satellite imagery and a spatiotemporal attention network," *IEEE Trans. Geosci. Remote Sens.*, vol. 61, pp. 1–18, 2023.
- [43] C. Li, X. Liu, and S. Li, "Transformer meets gan: Cloud-free multi-spectral image reconstruction via multi-sensor data fusion in satellite images," *IEEE Trans. Geosci. Remote Sens.*, 2023.
- [44] Z. Zhu and C. E. Woodcock, "Object-based cloud and cloud shadow detection in landsat imagery," *Remote Sens. Environ.*, vol. 118, pp. 83–94, 2012.
- [45] Z. Wang, A. C. Bovik, H. R. Sheikh, and E. P. Simoncelli, "Image quality assessment: from error visibility to structural similarity," *IEEE Trans. Image Process.*, vol. 13, no. 4, pp. 600–612, 2004.
- [46] K. Simonyan and A. Zisserman, "Very deep convolutional networks for large-scale image recognition," *arXiv preprint arXiv:1409.1556*, 2014.